Phase-field model of vascular tumor growth: Three-dimensional geometry of the vascular network and integration with imaging data

Jiangping Xu[a], Guillermo Vilanova[b,*], Hector Gomez[c,d,e]

[a]*School of Mechanical Engineering, Jiangsu University.*
301 Xuefu Road, Zhenjiang City, Jiangsu, China.

[b]*LaCàN, Universitat Politècnica de Catalunya-BarcelonaTech,*
Campus Nord, 08034 Barcelona, Spain.

[c]*School of Mechanical Engineering, Purdue University,*
585 Purdue Mall, West Lafayette, IN 47907, USA.

[d]*Weldon School of Biomedical Engineering, Purdue University,*
206 S. Martin Jischke Drive, West Lafayette, IN 47907, USA.

[e]*Purdue Center for Cancer Research, Purdue University,*
201 S. University Street, West Lafayette, IN 47907, USA.

Abstract

Tumors promote the growth of new capillaries through a process called angiogenesis. Blood flows through these new vessels providing cancerous cells with nutrients. However, because tumor-induced vasculature is defective, blood flow is heterogeneous both in space and time. As a result, regional hypoxia and acidosis may appear, increasing the malignancy of the tumor. In this work, we developed a three-dimensional model to address the complex interplay between angiogenesis, tumor growth, nutrient distribution and blood flow. The model emphasizes three-dimensional geometry of the vascular network and integration with *in vivo* imaging techniques by use of the phase-field approach. We show that our method allows computing directly on the photoacoustic imaging raw data, avoiding the mesh generation process, which is the usual bottleneck for integration of computational methods and imaging data. We present two- and three-dimensional results of the dynamics of vascular tumor growth coupled with blood flow within a time-evolving capillary network.

Keywords: Nutrient transport, Tumor growth, Angiogenesis, Computational modeling

1. Introduction

Malignant tumors are characterized by an accelerated and uncontrolled proliferation of their cells [1]. At the earliest stages of tumor evolution, cancerous cells feed from the blood delivered by the pre-existent capillaries. However, due to their high nutrient demands, the oxygen supply soon becomes scarce inside the tumor; hypoxic regions develop and cells enter quiescent or necrotic states, arresting the global growth of the lesion [2]. For the tumor to continue spreading, its cells need to find a way to overcome this natural

*Corresponding author:guillermo.vilanova@upc.edu

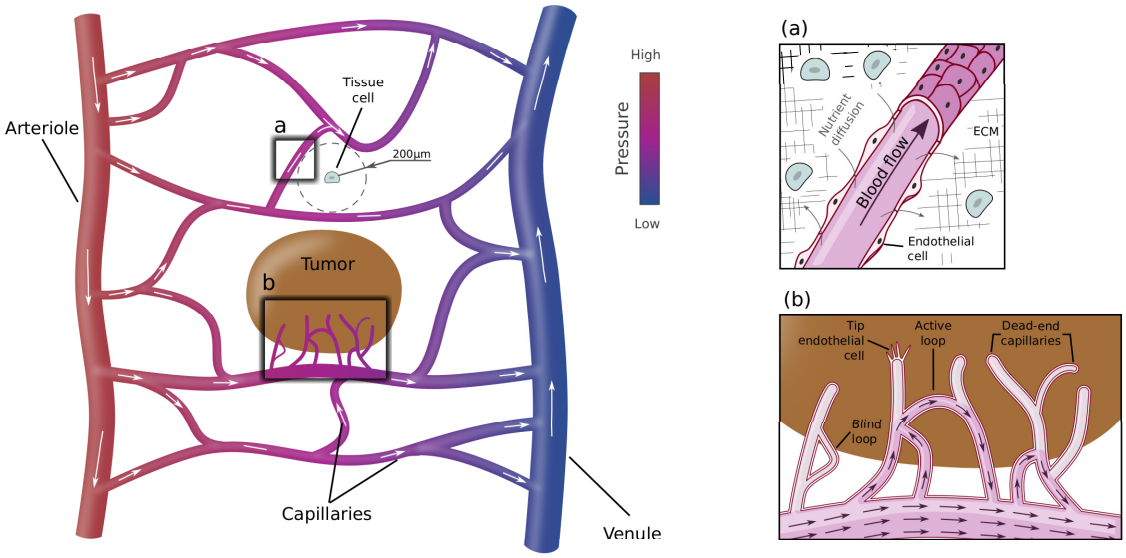

Figure 1. Blood circulation in the tumor microenvironment. Blood enters into capillaries from arterioles (high pressure) and leaves through venules (low pressure) in the microcirculatory system. (a) Nutrients extravasate capillaries and diffuse within the extracellular matrix (ECM). Nutrients reach cells within a $\sim 200\,\mu$m-range through the diffusion mechanism. (b) Solid tumors promote angiogenesis: the creation of new capillaries from pre-existing ones. Tip endothelial cells lead the growth of new capillaries. The neovascular network forms different structures as it evolves: dead-end capillaries, blind loops and active loops. Blood flows only through active loops oxygenating the surrounding host and tumoral tissue.

barrier. One way to accomplish this is promoting the growth of new blood vessels from the pre-existing ones [2]. Through this process, called *angiogenesis*, new capillaries sprout, grow and form a vascular network that provides extra nutrients and oxygen to cancerous cells, resuming the growth of the tumor [3]. However, the supply of nutrients to the tumor is tightly regulated by the blood flow dynamics in the tumor microenvironment; see Fig. 1. Tumor-induced vascular networks are structurally and functionally defective [4]. As shown in Fig. 1b, blood flow is heterogeneous in space, but also in time [5]. The flow is often redundant or impaired by dead-end capillaries and blind loops. Combined with the high tumoral interstitial pressure, this results in regional hypoxia and acidosis, which in turn increases the malignancy of tumors [6]. While the interaction between tumors and capillary networks has been the subject of much research, we are still far from understanding how capillary growth and remodeling, blood flow and oxygen exchange orchestrate tumor growth.

Computational modeling provides an opportunity to improve our mechanistic understanding of the interactions between nutrients, capillaries and cancerous cells in the tumor microenvironment, but it has only been used recently to study cancer-related biological processes [7–9]. Most models of vascular tumor growth couple a multidimensional continuum description of the tumor (e.g., a cellular density field [10] or a phase-field [11] that identifies the tumor) with a discrete vascular network where each rectilinear segment is approximated by one-dimensional Poiseuille flow with nonlinear rheology [12–15]. These models have provided significant insight into the mechanisms that control the coordinated growth of tumors and their associated microvascular networks. In our opinion, these models have two major strengths: The first one is that they incorporate important features of the non-Newtonian rheology of blood at the microcirculation scale. The dependence of the apparent viscosity on hematocrit and vessel diameter is incorporated fitting data from circulation in the rat mesentery [12–15]. The second strength of this approach is that the 1D

representation of the vascular network allows to incorporate in a straightforward manner vessel diameter adaptation, which has been postulated as one of the key mechanisms of vessel remodeling in the tumor microenvironment. The aforementioned 1D blood flow models have also been widely used in studies of cerebral flow, outside of cancer research. In the field of cerebral blood flow, efforts have been made to couple these 1D flow models with imaging data [16–18]. Although these attempts have been successful, the integration with imaging data requires manual segmentation of the vascular tree, which is exceedingly complicated.

More recently, several models of vascular tumor growth that include a 3D representation of the capillaries have been proposed [19, 20]. The microvascular network is represented by a phase field, which describes its geometry implicitly as the zero level set of a scalar function. This avoids the mesh generation of the vessel network, which is very difficult for a stationary network and practically impossible for a time-evolving network. The mesh update process in a time-evolving network would require mesh warping [21], but also re-meshing due to topological changes in the intravascular domain. Up to now, the focus of the aforementioned phase-field models [19, 20] has been to describe the time evolution of the capillary network. Therefore, they have not yet been coupled with flow compartments, what limits their ability to predict nutrient release accurately. Here, we address this gap by extending [19] with a flow compartment and simultaneously show that the 3D representation of the network provides a route for direct integration of the computational method with imaging data, avoiding altogether the segmentation of the vascular tree. Our results show that models of vascular tumor growth that describe the 3D geometry of the vessel network using a phase-field can be coupled to a flow dynamics model even when the geometry and topology of the network changes with time. Although our initial approach to model fluid flow is very simple and it is based on Darcy flow, it can be extended to Stokes [22] or Navier-Stokes flow with nonlinear rheology. We illustrate the capabilities of our method for direct integration with imaging data by performing a computation in which the initial geometry and topology of the vascular network is obtained from photoacoustic images.

The paper is organized as follows: Section 2 describes the mathematical model for vascular tumor growth including blood flow and angiogenesis, and how we exploit the phase field method to extract vascular network geometries from images. Section 3 gives the details of the computational method to solve the governing equations. Section 4 presents two- and three-dimensional simulations performed with the proposed model and using *in vivo* information taken from images. Finally, we discuss the results and draw conclusions in Section 5.

2. Mathematical model

2.1. Introduction to phase-field modeling

The phase-field method is a mathematical approach to describe problems with moving interfaces as partial differential equations (PDEs) posed on a fixed domain. It has been widely applied in the areas of phase transformations [23, 29], microstructure evolution [24], phase separation [25], solidification [26, 27], and fluid-structure interaction [30, 31] just to name a few. Another important area of application is the solution of PDEs in complex domains avoiding mesh generation [32]. In this context, the phase-field approach is usually called *diffuse domain method*. Although the details are different, the concept is similar to that of the finite cell method [33], embedded domain method [34], or ghost cell method [34]. The key idea of the phase-field method is to use a scalar field to define the location of different "phases", where phase may refer to materials, states of matter or the computational domain. Conceptually, this is similar to the level set approach [35] with two essential differences that have turned out to be crucial for the success of the phase-field method: First, the phase-field method naturally takes on a hyperbolic tangent

profile in the direction normal to the interface, which provides robustness in the computations, and second, phase-field models can often be derived from free-energy functionals using rigorous thermo-mechanical approaches, such as the Coleman-Noll procedure [36].

2.2. Mathematical model of vascular tumor growth

The process of vascular tumor growth is exceedingly complex [3, 37, 38]. One key element of it is that under hypoxic conditions (low oxygen), tumor cells release tumor angiogenic factors (TAFs) that reach the endothelial cells that line pre-existent capillaries. These growth factors change the phenotype of endothelial cells from quiescent to migratory or proliferative, starting the generation of a new capillary. Migratory endothelial cells, known as tip endothelial cells (TECs), lead the growth of neo-capillaries towards the source of TAFs, while proliferative endothelial cells or stalk cells elongate the vessel by cell division. As the capillary grows, a lumen is formed allowing blood to flow through it. However, it is not until the new vessel fuses its lumen with another one, in a process termed anastomosis, that blood can flow unconstrained. Nutrients and oxygen may now be released from the new capillary loop feeding the hypoxic tumor cells, and promoting local tumor growth. As new loops are formed, more tumor cells receive nutrients and oxygen resulting in an overall growth of the lesion.

Our model focuses on the heterogeneous distribution of blood flow in the dynamically changing vasculature that forms the microcirculation of a tumor. The key idea is that, by defining the location of capillaries through a phase-field, we can solve the flow dynamics equations in the whole computational domain rather than in the intricate capillary network sub-domain. This concept allows to simulate blood flow without meshing the capillaries every time there is a change in the vascular network and also introduces a way to simulate directly on imaging data, skipping the time-consuming, non-automatic process of meshing capillaries. In addition to blood flow and capillaries, the model considers several phenomena such as the limited delivery of nutrient due to abnormal blood flow, the local growth of a tumor based on the availability of nutrient and the pathological tumor-induced angiogenesis. To model these complex, intertwined phenomena we use a previous theory developed by the authors [39] but extended to incorporate the effect of blood flow. The main components of the model are the blood vessels, the tumor, the TAFs, the nutrients, and the TECs. Both the capillaries and the tumor are described by their cells' spatial location using the phase fields c and ϕ, respectively. We use reaction-diffusion equations to model the dynamics of the chemical substances TAF (f) and nutrient (σ). The concentrations f and σ are normalized to one.

2.2.1. Capillary growth

We use the order parameter $c \in [-1, 1]$ to describe the spatial location of capillaries, where $c \approx 1$ represents intravascular space and $c \approx -1$, the rest of the tissue, both host and tumoral. Due to the structure of the phase-field equations, the unknown c will transition smoothly from the value -1 to $+1$. The dynamics of the field c is governed by the equation

$$\frac{\partial c}{\partial t} = \nabla \cdot \left(M_c \nabla \left(\mu_c \left(c \right) - \lambda_c^2 \Delta c \right) \right) + \mathcal{B}_\mathrm{p} \left(f, \phi \right) c \mathcal{H} \left(c \right), \tag{1}$$

where M_c is a positive constant that represents the mobility of endothelial cells and λ_c is a length scale that defines the thickness of the capillary wall. The function $\mu_c(c) = c^3 - c$ is the derivative of the symmetric double-well potential $\Psi_c \left(c \right) = c^4/4 - c^2/2$ with local minima at $c = -1$ and $c = 1$. The term $\mathcal{B}_\mathrm{p}(f, \phi)$ represents the proliferation rate of endothelial cells as a function of TAF concentration and is expressed as

$$\mathcal{B}_\mathrm{p}(f, \phi) = \begin{cases} B_\mathrm{p}[1 - (1 - \epsilon_\phi)\phi] f & \text{if } f < f_\mathrm{p} \\ B_\mathrm{p}[1 - (1 - \epsilon_\phi)\phi] f_\mathrm{p} & \text{if } f \geq f_\mathrm{p} \end{cases}, \tag{2}$$

where f_{p} is the TAF concentration at which proliferation saturates to its maximum rate ($B_{\mathrm{p}} f_{\mathrm{p}}$) and B_{p} is the proliferative rate of endothelial cells in the host tissue. The term $[1 - (1 - \epsilon_\phi)\phi]$ accounts for the different proliferation of endothelial cells in the healthy tissue ($\phi \approx 0$) and the tumor tissue ($\phi \approx 1$). We took $\epsilon_\phi = 0.1$ in the simulations. Finally, $\mathcal{H}(\cdot)$ is a Heaviside function that localizes proliferation to the capillaries[1].

Tip endothelial cells are modeled as circular (2D) or spherical (3D), mesh-free, discrete agents of radius R. We incorporate this description of TECs with the continuous definition of endothelial cells by imposing $c = 1$ at the location of TECs, following the concept of templates [40]. TECs can get activated and deactivated, move following chemotactic gradients of TAF, spread filopodia, detect nearby capillaries, and anastomose with them. A new TEC is activated (deactivated) if the following conditions are met (not met) at a point:

1. $c \geq c_{\mathrm{act}}$, which guarantees that the point is inside a capillary;
2. $f \geq f_{\mathrm{act}}$, which establishes the minimum TAF concentration to trigger the activation; and
3. the distance to any other TEC is larger than δ_4, which mimics the lateral inhibition mechanism [41].

Each time step every TEC is moved with velocity $\mathbf{v}_{\mathrm{TEC}} = \chi \frac{\nabla f}{|\nabla f|}$. TECs can also project forward cytoplasmatic protrusions called filopodia that aid their movement towards the source of TAF [42]. Furthermore, they can also detect nearby capillaries through filopodia to form anastomoses. Following [43], after a TEC has migrated the equivalent of four radii away from its parent vessel, the discrete agent performs checks at points that represent the location of filopodia; see [40, 43] for more details on our modeling approach for TECs.

2.2.2. Blood flow

Developing an accurate computational model of blood flow in a time-evolving capillary network is an open research problem that is out of the scope of this paper [12–15]. Therefore we resort to a porous media flow model. The model can be easily extended to Stokes flow of a non-Newtonian fluid, but this is not addressed here. Our porous media flow model is given by

$$\nabla \cdot \mathbf{v} = 0, \tag{3}$$

$$\mathbf{v} = -\mathcal{K} \nabla p, \tag{4}$$

where $\mathbf{v}$ is the fluid velocity, p the fluid pressure and $\mathcal{K}$ is the normalized hydraulic conductivity of the medium. In order to restrict blood flow to capillaries we make use of the diffuse domain method [32]. Eq. (1) that governs the evolution of capillaries automatically produces a smooth transition layer between capillaries and the surrounding tissue. Thus, exploiting the smoothness of the phase field, we can derive a diffuse Darcy's law, in which the hydraulic conductivity depends on the value of c as follows:

$$\mathcal{K} = \mathcal{K}(c) = \begin{cases} \epsilon_\kappa & \text{if } c < -c^\star \\ \frac{1-\epsilon_\kappa}{2c^\star}(c + c^\star) + \epsilon_\kappa & \text{if } c \in [-c^\star, c^\star] \\ 1 & \text{if } c > c^\star \end{cases}, \tag{5}$$

where $c^\star = 1 - \epsilon_c$ (with $\epsilon_c = 0.02$) and $\epsilon_\kappa = 10^{-6}$ are computational parameters used to avoid singularities. According to Eq. (5), the conductivity decreases linearly with c producing smooth transitions across

[1] To improve the convergence rate of our algorithm, in practice, we replace the Heaviside function by a smooth approximation defined by a hyperbolic tangent.

capillary walls. Finally, using Eq. (5) and combining Eqs. (3) and (4) we obtain the following steady-state equation for the blood pressure:

$$\nabla \cdot (-\mathcal{K}(c)\,\nabla p) = 0. \tag{6}$$

Note that Eq. (6) is defined in the full computational domain rather than only in a sub-domain defined by the vasculature. Therefore, not only do we avoid the computationally intensive process of generating the mesh for the initial capillaries but also the prohibitive computational cost of changing the mesh as capillaries evolve due to angiogenesis. It can be shown that Eq. (6) is asymptotically equivalent to solving Eqs. (3) and (4) in the capillary network with constant hydraulic conductivity; see [32].

2.2.3. Nutrient transport

Tumor growth is supported by nutrients that extravasate from capillaries, including oxygen, glucose, amino acids and fatty acids. Taking into account that nutrients are released from perfused capillaries, diffuse through the extravascular tissue and are consumed both by cancerous and host cells at different rates, we model this process with the reaction-diffusion equation

$$\frac{\partial \sigma}{\partial t} = \nabla \cdot (D_\sigma \nabla \sigma) + V_{\mathrm{p}}^{\mathrm{C}}\,(p - p_{\mathrm{i}})\,\alpha(\sigma)\,c\mathcal{H}(c) - V_{\mathrm{u}}^{\mathrm{T}}\sigma\phi - V_{\mathrm{u}}^{\mathrm{H}}\sigma\mathcal{H}(1-\phi), \tag{7}$$

where D_σ is the diffusion constant of the nutrient, $V_{\mathrm{p}}^{\mathrm{C}}$ is the permeability of the capillary, p is the intravascular pressure, p_{i} is the interstitial pressure, whereas $V_{\mathrm{u}}^{\mathrm{T}}$ and $V_{\mathrm{u}}^{\mathrm{H}}$ are the uptake rates of nutrient by tumoral and host tissue, respectively. Here, we assume that the host tissue and the capillaries have the same uptake rate of nutrient. The second term on the right-hand side models nutrient transfer from capillaries to tissue interstitium following an expression analogous to Starling's law for negligible influence of the osmotic pressure [44, 45]. We further assume that the (gage) pressure in the interstitium is constant and equal to zero. In addition, this transfer is proportional to

$$\alpha(\sigma) = \begin{cases} \epsilon_\sigma & \text{if } |\mathbf{v}| \leqslant v_{\mathrm{p}} \\ 1-\sigma & \text{if } |\mathbf{v}| > v_{\mathrm{p}} \end{cases}, \tag{8}$$

where ϵ_σ is a small positive constant and v_{p} is a threshold velocity used to differentiate well and poorly perfused capillaries. As a result, if blood scarcely flows through a capillary, such as in dead-end capillaries, its nutrient supply is reduced to a residual value ϵ_σ.

2.2.4. Tumor growth

Analogously to the description of capillaries, we use a phase-field $\phi \in [0, 1]$ to describe the tumor ($\phi \approx 1$) and the host tissue ($\phi \approx 0$) phases. The dynamics of ϕ is governed by the non-conserved phase-field equation

$$\frac{\partial \phi}{\partial t} = M_\phi \left(\lambda_\phi^2 \Delta\phi - \mu_\phi(\phi, \sigma)\right), \tag{9}$$

that models tumor growth or shrinkage as a function of nutrient availability and generates smooth transition layers at the tumor boundaries. In Eq. (9), M_ϕ is a positive constant representing the tumor mobility and λ_ϕ is a length scale proportional to the thickness of the diffuse interface between the tumor and the host tissue. The function μ_ϕ is the derivative of a double-well potential Ψ_ϕ, which has two local minima at $\phi = 0$ and $\phi = 1$ and is defined as

$$\Psi_\phi(\phi, \sigma) = \phi^2(1-\phi)^2 + m(\sigma)\,\phi^2(3 - 2\phi). \tag{10}$$

Here, the first term is a symmetric double-well potential with two local minima at $\phi = 0$ and $\phi = 1$, while the second term introduces a non-symmetric perturbation. The function $m(\sigma)$, called tilting function in the phase-field literature, is defined as

$$m(\sigma) = \epsilon_m - \frac{1}{6} + \frac{1}{6} \tanh \frac{\sigma^* - \sigma}{\sigma^{\mathrm{s}}}, \tag{11}$$

where ϵ_m is a small positive constant, σ^* is the inflection point of $m(\sigma)$ and σ^{s} defines the slope of the function. In order to obtain local minima at $\phi = 0$ and $\phi = 1$ for Ψ_ϕ, the value of the parameters of the function $m(\sigma)$ are taken to verify $|m(\sigma)| < 1/3$ for all σ (see [46] for details). As a result, Ψ_ϕ energetically favors one of the two metastable solutions ($\phi = 0$ or $\phi = 1$) depending on the value of σ. Eqs. (10) and (11) are standard in the phase field literature [46].

2.2.5. Tumor angiogenic factor dynamics

In the absence of enough nutrients, tumors release TAFs to trigger angiogenesis. There is evidence of a wide range of TAFs [47–49], both with pro- and anti-angiogenic effects. In this work we use a dimensionless variable f that represents the balance between these factors, so that larger values of f indicate a pro-angiogenic tendency. We model the dynamics of f using the reaction-diffusion equation

$$\frac{\partial f}{\partial t} = \nabla \cdot \left(D_f \nabla f \right) + \phi \left(1 - f\right) \mathcal{G}\left(\sigma\right) - B_{\mathrm{u}} f c \mathcal{H}\left(c\right) - \delta f, \tag{12}$$

where D_f is the diffusion constant of TAF, $\mathcal{G}(\sigma)$ is the secretion rate of TAF by tumor cells, B_{u} is the uptake rate of TAF by endothelial cells and δ is the natural decay rate of TAF. In order to reflect the experimentally-proven fact that TAF is mainly released by hypoxic tumor cells, we define $\mathcal{G}(\sigma)$ as a hill function of σ that achieves a maximum at $\sigma = (\sigma^{\text{n-h}} + \sigma^{\text{h-v}})/2$ and decreases quickly away from this value. $\sigma^{\text{n-h}}$ and $\sigma^{\text{h-v}}$ are the values of the nutrient concentration that define the threshold between necrotic and hypoxic tumor cells and between hypoxic and viable cells, respectively. The expression of $\mathcal{G}(\sigma)$ used in this work is given by

$$\mathcal{G}(\sigma) = \mathcal{G}_{\mathrm{ref}} \exp\left(- \left(\frac{\sigma - (\sigma^{\text{n-h}} + \sigma^{\text{h-v}})/2}{\sigma^{\mathcal{G}}_{\mathrm{ref}}} \right)^2 \right), \tag{13}$$

where $\mathcal{G}_{\mathrm{ref}}$ and $\sigma^{\mathcal{G}}_{\mathrm{ref}}$ are reference values defined in Appendix A.

2.3. Image-based geometry extraction

A necessary step to perform simulations using *in vivo* information is to transform images into data that can be used as an input for the model. For angiogenesis models, in particular, the geometry of the capillaries is of special relevance. Typically, capillaries are idealized in the models as their middle line or, in the exceptional cases that pursue three-dimensional modeling, by their exterior surface [50]. Thus, the workflow from the image acquisition and segmentation to its use in the model requires the skeletonization of the vessels [51] or the meshing of their surface. These two last processes are very difficult and time-consuming, usually representing a bottleneck in the extraction of the geometry. Our model, however, can directly use the raw data coming from the binarization of the image, avoiding these expensive operations: The binary data is directly stored into the phase-field variable c and scaled so that $c = 1$ represents intravascular space in the image and $c = -1$, the complementary space. The same procedure can be used for the tumor location.

In some cases, the image resolution (or the number of slices in the stack) may not suffice to store directly the scaled binary data into the phase-field variable. Therefore when the model needs to be fed

from low-resolution 3D data we use the following strategy: After storing the data from the binarized image into c_s, we evolve in time the equation

$$\frac{\partial c_s}{\partial t} = \nabla \cdot \left(\nabla \left(\mu_c \left(c_s \right) - \lambda_c^2 \Delta c_s \right) \right) \tag{14}$$

up to $t = t^\star$. Note that the function μ_c and the constant λ_c are the same as in Eq. (1). By evolving Eq. (14) up to a small time $t^\star$, the sharp transition present in the binary image acquires a smooth hyperbolic tangent profile and the interface length decreases slightly getting rid of small unimportant features. The resulting field $c_s(t^\star)$ can be directly used as an input of the model.

3. Computational method

The proposed model is highly nonlinear, with a strong coupling between the different equations and includes dynamic and stationary PDEs. The phase fields representing the capillaries and the tumor develop thin layers that need to be resolved by the computational mesh. Also, the PDE describing vascular growth includes higher-order derivatives that require C^1 elements in a finite element formulation. To handle these computational challenges, we used isogeometric analysis (IGA), which has proven very successful for phase-field equations; see [52, 53]. The values of the parameters used in the simulations are described in Appendix A.

3.1. Governing equations

Define the computational domain $\Omega \subset \mathbb{R}^d$ ($d = 2$ or 3) and its boundary Γ. The unit vector $\boldsymbol{n}$ is a well-defined outward normal to Ω. The time interval of computation is $\mathcal{I} = (0, T)$. The problem can be stated as: given suitable initial conditions, find p, ϕ, c, f and σ such that

$$\nabla \cdot \left(-\mathcal{K}\left(c\right) \nabla p \right) = 0, \tag{15}$$

$$\frac{\partial \phi}{\partial t} = M_\phi \left(\lambda_\phi^2 \Delta \phi - \mu_\phi(\phi, \sigma) \right), \tag{16}$$

$$\frac{\partial c}{\partial t} = \nabla \cdot \left(M_c \nabla \left(\mu_c \left(c \right) - \lambda_c^2 \Delta c \right) \right) + \mathcal{B}_p \left(f, \phi \right) c \mathcal{H}\left(c \right), \tag{17}$$

$$\frac{\partial f}{\partial t} = \nabla \cdot \left(D_f \nabla f \right) + \phi \left(1 - f \right) \mathcal{G}\left(\sigma \right) - B_u f c \mathcal{H}\left(c \right) - \delta f, \tag{18}$$

$$\frac{\partial \sigma}{\partial t} = \nabla \cdot \left(D_\sigma \nabla \sigma \right) + V_{\mathrm{p}}^{\mathrm{C}} \left(p - p_{\mathrm{i}} \right) \alpha \left(\sigma \right) c \mathcal{H}(c) - V_{\mathrm{u}}^{\mathrm{T}} \sigma \phi - V_{\mathrm{u}}^{\mathrm{H}} \sigma \mathcal{H}(1 - \phi) \tag{19}$$

in $\Omega \times (0, T)$ and satisfying the following boundary conditions:

$$\mathcal{K}\left(c\right) \nabla p \cdot \boldsymbol{n} = 0 \quad \text{on} \quad \Gamma \times (0, T), \tag{20}$$

$$\nabla \phi \cdot \boldsymbol{n} = 0 \quad \text{on} \quad \Gamma \times (0, T), \tag{21}$$

$$\nabla \left(\mu_c(c) - \lambda_c^2 \Delta c \right) \cdot \boldsymbol{n} = 0 \quad \text{on} \quad \Gamma \times (0, T), \tag{22}$$

$$\Delta c = 0 \quad \text{on} \quad \Gamma \times (0, T), \tag{23}$$

$$\nabla f \cdot \boldsymbol{n} = 0 \quad \text{on} \quad \Gamma \times (0, T), \tag{24}$$

$$\nabla \sigma \cdot \boldsymbol{n} = 0 \quad \text{on} \quad \Gamma \times (0, T). \tag{25}$$

As mentioned in subsection 2.2.1 the field c is not only governed by the continuous Eq. (17), but it is also updated dynamically to account for the migration of TECs.

3.2. Spatial discretization

Let us define the trial and weighting function spaces $\mathcal{V} \subset \mathcal{H}^2(\Omega)$. Here, $\mathcal{H}^2(\Omega)$ is the Sobolev space of square integrable functions with square integrable first and second derivatives in the domain Ω. The requirement $\mathcal{V} \subset \mathcal{H}^2(\Omega)$ is motivated by the fourth-order derivatives of the unknown c in Eq. (1). For simplicity, we will use the same functional space for all unknowns even if standard $\mathcal{H}^1$-conforming spaces would suffice for the unknowns p, ϕ, f and σ. The finite-dimensional space for discretization is defined as $\mathcal{V}^h = \text{span}\{N_A\}_{A=1,\dots,n_b}$, where n_b is the dimension of $\mathcal{V}^h$ and the N_A's are linearly independent spline basis functions. The use of IGA permits us to generate basis functions with controllable continuity across element boundaries. For example, by taking C^1-continuous quadratic splines, the requirement $\mathcal{V}^h \subset \mathcal{V} \subset \mathcal{H}^2(\Omega)$ is automatically satisfied.

Multiplying the governing equations with weighting functions, integrating by parts [twice for Eq. (17)] and applying the Galerkin method, we obtain the following discrete variational problem: find $\{p^h, \phi^h, c^h, f^h, \sigma^h\} \in \mathcal{V}^h$ such that for all $\{w_p^h, w_\phi^h, w_c^h, w_f^h, w_\sigma^h\} \in \mathcal{V}^h$:

$$\left(\nabla w_p^h, \mathcal{K}\left(c^h\right)\nabla p^h\right)_\Omega = 0, \tag{26}$$

$$\left(w_\phi^h, \frac{\partial \phi^h}{\partial t}\right)_\Omega + \left(\nabla w_\phi^h, M_\phi \lambda_\phi^2 \nabla \phi^h\right)_\Omega + \left(w_\phi^h, M_\phi \mu_\phi(\phi^h, \sigma^h)\right)_\Omega = 0, \tag{27}$$

$$\left(w_c^h, \frac{\partial c^h}{\partial t}\right)_\Omega + \left(\nabla w_c^h, M_c \nabla \mu_c(c^h)\right)_\Omega + \left(\Delta w_c^h, M_c \lambda_c^2 \Delta c^h\right)_\Omega - \left(w_c^h, \mathcal{B}_p\left(f^h, \phi^h\right) c^h \mathcal{H}\left(c^h\right)\right)_\Omega = 0, \tag{28}$$

$$\left(w_f^h, \frac{\partial f^h}{\partial t}\right)_\Omega + \left(\nabla w_f^h, D_f \nabla f^h\right)_\Omega + \left(w_f^h, B_u f^h c^h \mathcal{H}\left(c^h\right)\right)_\Omega + \left(w_f^h, \delta f^h\right)_\Omega - \left(w_f^h, \phi^h(1 - f^h)\mathcal{G}(\sigma^h)\right)_\Omega = 0, \tag{29}$$

$$\left(w_\sigma^h, \frac{\partial \sigma^h}{\partial t}\right)_\Omega + \left(\nabla w_\sigma^h, D_\sigma \nabla \sigma^h\right)_\Omega + \left(w_\sigma^h, V_u^T \sigma^h \phi^h + V_u^H \sigma^h \mathcal{H}(1 - \phi^h) - V_p^c\left(p^h - p_\text{i}\right)\alpha\left(\sigma^h\right) c^h \mathcal{H}\left(c^h\right)\right)_\Omega = 0, \tag{30}$$

where $(\cdot,\cdot)_\Omega$ is the $\mathcal{L}^2$ inner product in the domain Ω. The discrete solution p^h is defined as

$$p^h(\boldsymbol{x}, t) = \sum_{A=1}^{n_b} p_A(t)\, N_A(\boldsymbol{x}), \tag{31}$$

where the p_A's are the control variables. The remaining unknowns $\phi^h(\boldsymbol{x}, t)$, $c^h(\boldsymbol{x}, t)$, $f^h(\boldsymbol{x}, t)$ and $\sigma^h(\boldsymbol{x}, t)$ are defined similarly. The weight function w_p^h is expressed as

$$w_p^h(\boldsymbol{x}) = \sum_{A=1}^{n_b} w_{p,A}\, N_A(\boldsymbol{x}). \tag{32}$$

The weight functions w_ϕ^h, w_c^h, w_f^h and w_σ^h are defined analogously.

3.3. Time discretization

Because the flow equation is stationary and the remaining equations are unsteady, we propose a staggering scheme. We explored several options and obtained the most accurate and stable results solving the pressure field first, using the vascular network from the previous time step. The dynamic equations are approximated using the generalized-α method [54]. We use the notation $\boldsymbol{P}_n$, $\boldsymbol{\Phi}_n$, $\boldsymbol{C}_n$, $\boldsymbol{F}_n$ and $\boldsymbol{\Sigma}_n$ for the global vector of control variables of the unknowns p_n^h, ϕ_n^h, c_n^h, f_n^h and σ_n^h, where the subscript n refers to the time step. We call $\dot{\boldsymbol{P}}_n$, $\dot{\boldsymbol{\Phi}}_n$, $\dot{\boldsymbol{C}}_n$, $\dot{\boldsymbol{F}}_n$, and $\dot{\boldsymbol{\Sigma}}_n$ the time derivatives of the control variable vectors. We further introduce $\boldsymbol{S}_n = \{\boldsymbol{\Phi}_n, \boldsymbol{C}_n, \boldsymbol{F}_n, \boldsymbol{\Sigma}_n\}^T$. Using this notation, the residual vectors are defined as

$$R_A^P(\boldsymbol{P}_{n+1}, \boldsymbol{S}_n) = \left(\nabla N_A, \mathcal{K}\left(c_n^h\right)\nabla p_{n+1}^h\right)_\Omega, \tag{33}$$

$$R_A^\phi\left(\boldsymbol{S}_{n+\alpha_f}, \dot{\boldsymbol{S}}_{n+\alpha_m}\right) = \left(N_A, \dot{\phi}_{n+\alpha_m}^h\right)_\Omega + \left(\nabla N_A, M_\phi \lambda_\phi^2 \nabla \phi_{n+\alpha_f}^h\right)_\Omega + \left(N_A, M_\phi \mu_\phi\left(\phi_{n+\alpha_f}^h, \sigma_{n+\alpha_f}^h\right)\right)_\Omega, \tag{34}$$

$$\begin{aligned} R_A^c\left(\boldsymbol{S}_{n+\alpha_f}, \dot{\boldsymbol{S}}_{n+\alpha_m}\right) = &\left(N_A, \dot{c}_{n+\alpha_m}^h\right)_\Omega + \left(\nabla N_A, M_c \nabla \mu_c\left(c_{n+\alpha_f}^h\right)\right)_\Omega + \left(\Delta N_A, M_c \lambda_c^2 \Delta c_{n+\alpha_f}^h\right)_\Omega \\ &- \left(N_A, \mathcal{B}_p\left(f_{n+\alpha_f}^h, \phi_{n+\alpha_f}^h\right) c_{n+\alpha_f}^h \mathcal{H}\left(c_{n+\alpha_f}^h\right)\right)_\Omega, \end{aligned} \tag{35}$$

$$\begin{aligned} R_A^f\left(\boldsymbol{S}_{n+\alpha_f}, \dot{\boldsymbol{S}}_{n+\alpha_m}\right) = &\left(N_A, \dot{f}_{n+\alpha_m}^h\right)_\Omega + \left(\nabla N_A, D_f \nabla f_{n+\alpha_f}^h\right)_\Omega + \left(N_A, B_u f_{n+\alpha_f}^h c_{n+\alpha_f}^h \mathcal{H}\left(c_{n+\alpha_f}^h\right)\right)_\Omega + \left(N_A, \delta f_{n+\alpha_f}^h\right)_\Omega \\ &- \left(N_A, \phi_{n+\alpha_f}^h\left(1 - f_{n+\alpha_f}^h\right)\mathcal{G}\left(\sigma_{n+\alpha_f}^h\right)\right)_\Omega, \end{aligned} \tag{36}$$

$$\begin{aligned} R_A^\sigma\left(\boldsymbol{S}_{n+\alpha_f}, \dot{\boldsymbol{S}}_{n+\alpha_m}\right) = &\left(N_A, \dot{\sigma}_{n+\alpha_m}^h\right)_\Omega + \left(\nabla N_A, D_\sigma \nabla \sigma_{n+\alpha_f}^h\right)_\Omega + \left(N_A, V_u^T \sigma_{n+\alpha_f}^h \phi_{n+\alpha_f}^h + V_u^H \sigma_{n+\alpha_f}^h \mathcal{H}\left(1 - \phi_{n+\alpha_f}^h\right)\right)_\Omega \\ &- \left(N_A, V_p^c\left(p_{n+1}^h - p_i\right)\alpha\left(\sigma_{n+\alpha_f}^h\right) c_n^h \mathcal{H}\left(c_{n+\alpha_f}^h\right)\right)_\Omega, \end{aligned} \tag{37}$$

where

$$\dot{\boldsymbol{S}}_{n+\alpha_m}^h = \dot{\boldsymbol{S}}_n^h + \alpha_m\left(\dot{\boldsymbol{S}}_{n+1}^h - \dot{\boldsymbol{S}}_n^h\right), \tag{38}$$

$$\boldsymbol{S}_{n+\alpha_f}^h = \boldsymbol{S}_n^h + \alpha_f\left(\boldsymbol{S}_{n+1}^h - \boldsymbol{S}_n^h\right), \tag{39}$$

$$\boldsymbol{S}_{n+1}^h = \boldsymbol{S}_n^h + \Delta t_n \dot{\boldsymbol{S}}_n^h + \gamma \Delta t_n\left(\dot{\boldsymbol{S}}_{n+1}^h - \dot{\boldsymbol{S}}_n^h\right). \tag{40}$$

Following [54], we take

$$\alpha_m = \frac{1}{2}\left(\frac{3-\rho_\infty}{1+\rho_\infty}\right); \quad \alpha_f = \frac{1}{1+\rho_\infty}; \quad \gamma = \frac{1}{2} + \alpha_m - \alpha_f \quad \text{where} \quad \rho_\infty = 1/2. \tag{41}$$

Our staggering scheme can be defined as follows: We first obtain $\boldsymbol{P}_{n+1}$ solving the quasi-linear Eq. (33). Substituting $\boldsymbol{P}_{n+1}$ into (34)–(37) as appropriate, we obtain a nonlinear system for $\boldsymbol{S}_{n+1}$ that we linearize using the Newton-Raphson method.

4. Numerical simulations

4.1. Unifocal tumor surrounded by a perfused vessel

Here, we study the growth of an initially circular tumor surrounded by a capillary as shown in Fig. 2a. We assume that the tumor is hypoxic at time $t = 0$ d and that it has not released any TAF yet. Because the pressures cannot be easily estimated from imaging data, we use an arbitrary pressure scale setting blood pressures at the inlet and outlet of the capillary to $p_{\text{in}} = 1$ and $p_{\text{out}} = 0$, respectively.

We show in Fig. 2b the first stage of the simulation in which the tumor area decreases slightly. As the tumor is initially hypoxic, it releases TAF (green color) that diffuses throughout the domain. Once the TAF reaches the pre-existing capillary it triggers the angiogenesis cascade. In the figure, four sprouts have started their growth from the left-hand side and direct their migration towards the tumor (plotted as a contour line of $\phi = 0.5$) guided by TAF gradients. The distribution of TAF is altered by the new growing capillaries (Fig. 2c) which consume angiogenic factors. Eventually, there is not enough TAF to trigger the activation of more capillaries from the parent vessel. At this point, although the tumor has started the angiogenic process, it shrinks at a slow rate. The new capillaries only release a small amount of extra nutrient to the tumor because they are dead ends of the vasculature that are unable to carry blood.

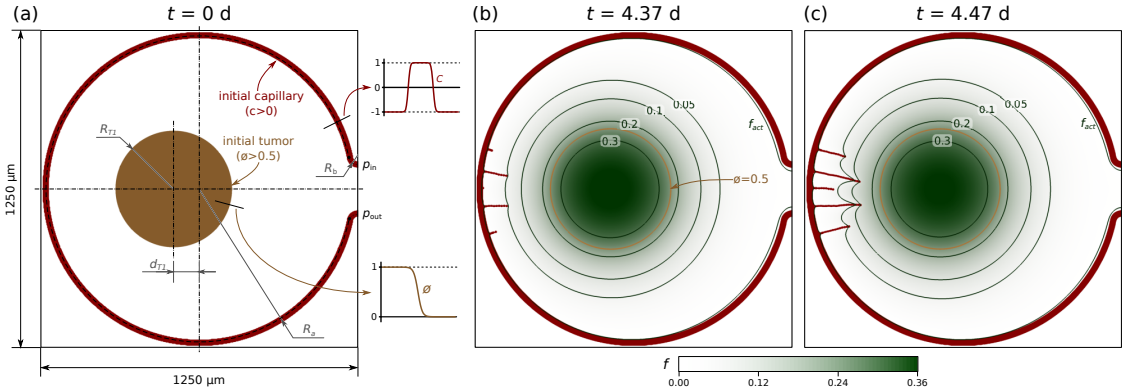

Figure 2. Initial configuration and snapshots at early times of the evolution of a unifocal tumor surrounded by a perfused vessel. (a) The computational domain represents a 1250 µm × 1250 µm square tissue which we discretize with a uniform computational mesh composed of 512 × 512 C^1-quadratic elements. The tumor's radius is $R_{\mathrm{T1}} = 247.5$ µm. Its center is at the horizontal central line and at a distance $d_{\mathrm{T1}} = 90$ µm from the center of the tissue. The initial capillary is composed of three arcs (dashed black line). The bigger arc (radius $R_{\mathrm{a}} = 606$ µm) is tangent to the other two arcs (same radius $R_{\mathrm{b}} = 32.5$ µm). The centers of the smaller arcs are both located at the right edge of the domain. The diameter of the vessel is 25 µm. As shown in the insets, both the tumor and the capillary are initially defined using smooth hyperbolic tangent profiles. (b)–(c) TAF distribution, TAF's contour lines (black solid line) at different levels and tumor contour (brown color) at $t = 4.37$ d and $t = 4.47$ d.

The shrinkage phase stops when the new sprouts connect among themselves creating a looped vasculature. In Fig. 3a-c we show snapshots of this situation at three different times, plotting the pressure, velocity and nutrient concentration in each row, respectively, along with the contour line $\phi = 0.5$ that represents the tumor boundary. At time $t = 6.50$ d there are three main vascular trees separated in Fig. 3a with dashed black lines. The upper and lower trees have only one connection with the initial vessel and consequently their pressure is uniform along each one as shown by the color scale. The middle and bottom rows of Fig. 3a show how their blood velocity is negligible compared to that of other parts of the vasculature; their nutrient release rate is also minimum. The situation is different in the central part of the neovasculature. Although the capillaries, represented by the zero level set of c, are not strictly connected to each other, the diffuse representation of the geometry leads to blood flow. This feature is inherent to the diffuse domain formulation and can be avoided taking smaller values of λ_c in Eq. (1), but this would require a finer computational mesh. The blood velocity through these central vessels is high enough to augment the discharge of nutrients to the tissue; see Eq. (8). Indeed, the tumor has used these nutrients to grow locally at that region. As the capillary network continues growing and branching, new anastomoses interconnect the vasculature. In contrast with dead-end capillaries and blind loops, these connections facilitate the passage of blood. By time $t = 6.83$ d (Fig. 3b) blood is flowing through all the capillaries that sprout from the parent vessel, although approximately half of the network is still formed by dead-end capillaries. By the end of the simulation, the continuous release of TAF from the hypoxic cells on the right-hand side of the lesion eventually promotes the full vascular enclosure of the tumor. At this point, a major loop that surrounds the tumor is releasing enough nutrient to sustain a fast growth of the tumor (Fig. 3c).

Figs. 3d-g highlight the evolution of the tumor and its three distinct regions: necrotic, hypoxic and proliferative. We defined these regions simply using threshold values of the nutrient concentration, namely, $\sigma^{\mathrm{n\text{-}h}}$ and $\sigma^{\mathrm{h\text{-}v}}$. Because the regions are defined based on the current nutrient distribution and do not refer to a phenotype of cancerous cells, a region that was considered necrotic at a certain time can, in principle, become hypoxic or normoxic later. In Fig. 3d, the majority of the cancerous cells are in the necrotic

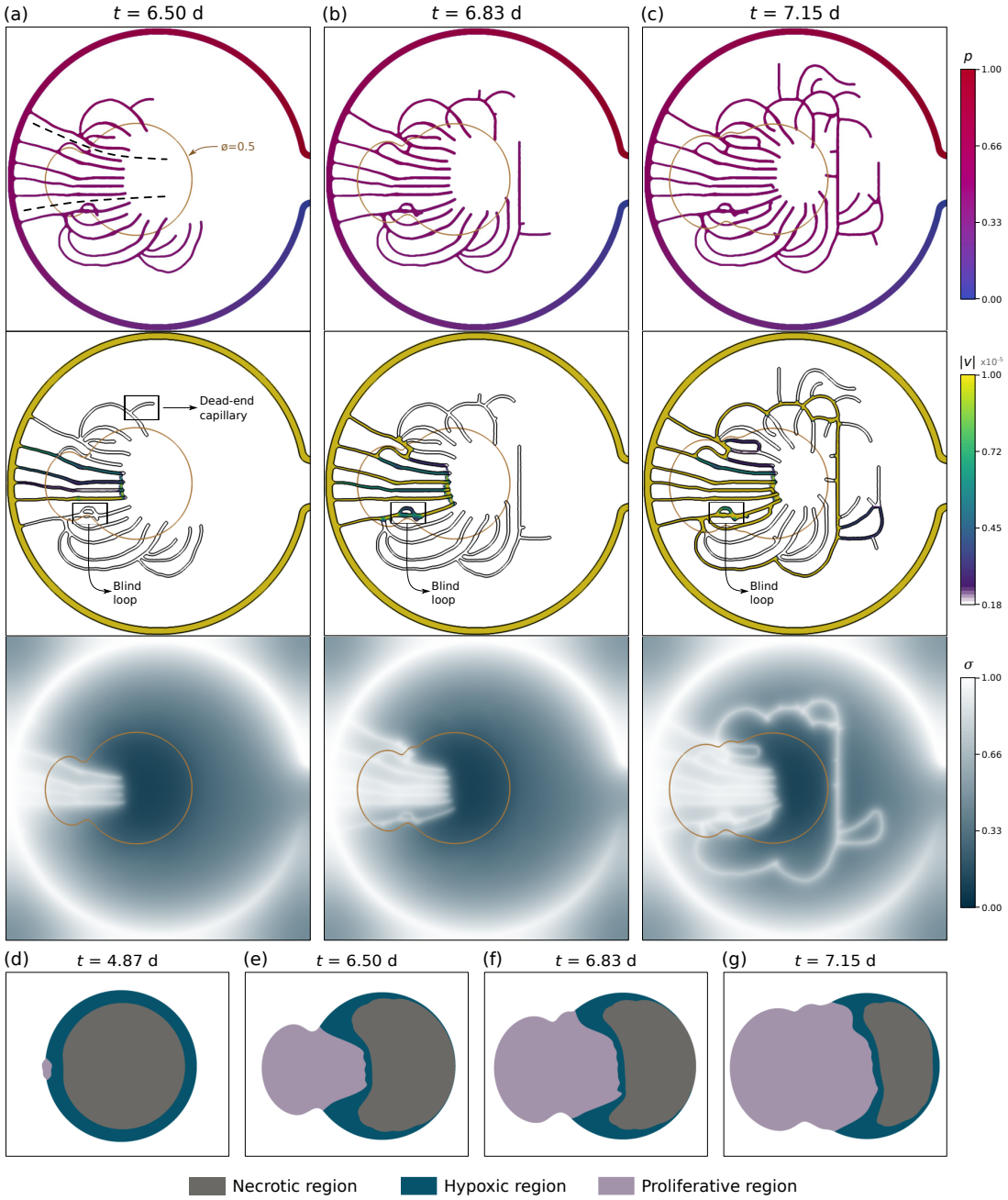

Figure 3. Evolution of a unifocal tumor surrounded by a perfused vessel. (a)–(c) Time evolution of the pressure (top row), velocity magnitude (middle row) and nutrient distribution (bottom row) along with the contour of the tumor (brown color). Note that the color scale for velocity is set to white when $|\boldsymbol{v}| < v_{\mathrm{p}}$. The dashed black lines separate three initial vascular trees. The pressure within the top and bottom trees is constant, while the middle one has a pressure gradient which leads to blood flow. The insets in the figures highlight dead-end capillaries in which there is no flow and blind loops in which the flow is low. As time evolves, the vasculature gets connected and more nutrient is released to the tissue. (d)–(g) Proliferative, hypoxic and necrotic regions of the tumor. The increase in nutrient promotes proliferation and reduction of the necrotic region.

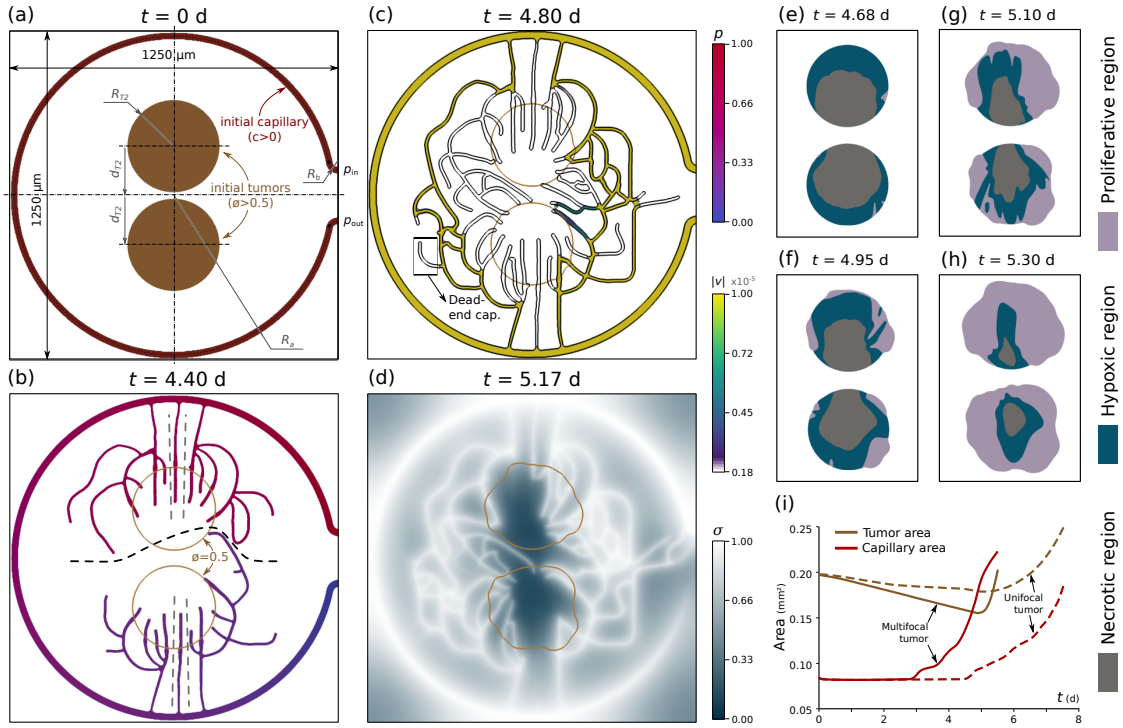

Figure 4. Initial configuration and evolution of a multifocal tumor enclosed by a blood-carrying capillary. (a) Initial configuration showing a parent capillary and two tumors. The center of each tumor is located along the vertical center line of the domain and at a distance $d_{T2} = 375\,\mu$m from the horizontal center line. Their radius is $R_{T2} = 175\,\mu$m, such that their combined volume is equal to that of the tumor in Fig. 2. (b) Pressure distribution within the capillaries at $t = 4.40$ d along with the tumor contour (brown color). The dashed lines split the new network into 6 unconnected vascular trees. Each tree has constant pressure. (c) Velocity magnitude of blood at $t = 4.80$ d. The new vasculature has two major paths through which blood can flow. The inset highlights a dead-end capillary. The color scale for velocity is set to white when $|v| < v_p$. (d) Nutrient distribution in the tissue at $t = 5.17$ d. The tumors are surrounded by a fully functional network that releases nutrient and boosts their growth. (e)–(h) Snapshots of the proliferative, hypoxic and necrotic regions of the tumors. (i) Plots of the area evolution of the capillaries and the tumor for this simulation (solid lines) and for the unifocal tumor (dashed lines).

region. Only those at the periphery are hypoxic and a small cluster on the left-hand side are proliferating. This cluster gets bigger as the new vasculature provides more nutrients, while the necrotic region shrinks and moves towards the right hand side of the tumor. At the same time, hypoxic cells are progressively pushed to the right side around the necrosis. The evolution of Figs. 3d-g shows how the tumor starts its growth from a small area close to the initial capillary that eventually occupies a significant part of the tumor. This leads to overall growth of the tumor and invasion of the surrounding tissue.

4.2. Multifocal tumor enclosed by a blood-carrying capillary

Here, we study a situation that is similar to that analyzed in section 3.1, but the tumor is now multifocal; see Fig. 4a. We study how the different tumor foci may cooperate to augment their chances of growth.

In our simulation, one tumor is closer to the upper part of the pre-existing capillary and the second one, to the lower part. Angiogenesis starts from these regions, which have a marked pressure difference. The fluid pressure is transmitted through the yet unconnected neovascular trees being constant within

each tree, as shown in Fig. 4b. When the capillaries of two trees anastomose, blood starts to flow through them. This is the case for the snapshot shown in Fig. 4c, where blood flows from the top to the bottom through two main routes that surround the tumors. The flow allows the irrigation of the tissue. However, at this point, there is still not enough nutrient inside the tumors to allow a fast growth due to the high nutrient consumption rate of cancerous cells. As time evolves, new capillaries generate more arterio-venous connections that eventually pervade the tumors. At time $t = 5.17\,\mathrm{d}$ (Fig. 4d) the new vasculature has provided large amounts of nutrient to the interior of the tumors. Figs. 4e-h show the evolution of the different regions of the tumors. Interestingly, the patterns are more complex than those of the previous simulation with only one tumor, due to the intricate orientation of capillaries. The tumors, which were initially hypoxic, rapidly develop a necrotic core almost completely enveloped by a hypoxic region. Due to the proximity of the initial capillaries and their input of nutrients, the necrotic cores are shifted towards the center of the domain. The switch to a vascular tumor is clear in the figures: First, the tumors grow locally in small areas located in the periphery (Fig. 4e). Then, as new capillaries surround and penetrate the tumor, more cells become proliferative while the necrosis gradually decreases (Figs. 4f-g). Throughout the process, hypoxic cells continue releasing TAF that keeps capillaries growing. At the end, the whole boundary of one tumor and most of the other one is occupied by proliferative cells (Fig. 4h). As the simulation evolves, the tumors transition from a hypoxic state to a well-defined, concentric structure.

In Fig. 4i we compare the evolution of tumor and capillary area in the two simulations presented so far. In both cases all tumors undergo slight shrinkage at the beginning due to the insufficient initial availability of nutrients. One difference between the simulations is that although the initial tumor areas are the same, the tumor boundary lengths are different. Thus, before angiogenesis is triggered, the multifocal tumor exhibits a faster shrinkage than the unifocal tumor (in our approach, tumors grow or shrink only at their boundaries). Angiogenesis starts later when the tumor is unifocal, due to the smaller quantity of TAF and the separation from the initial network. However, this fact does not delay tumor growth notably. We find that significant tumor growth starts at similar times: At 4.85 d for the unifocal tumor and at 4.74 d for the multifocal tumor. The main reason for this is that in the former case the vascular network gets connected faster than in the latter case. Once angiogenesis has been triggered and the vasculature is connected, tumors grow at high but different rates, for two main reasons: First, the unifocal tumor has a lower interfacial length; second, the neovasculature of the multifocal tumor connects regions with higher pressure differences, which promotes better irrigation of the tumors. As a result, the average growth rate of the multifocal tumor is 7.67 times higher.

Nutrient release and uptake play an important role in the evolution of the tumor. In order to study them, we define nutrient release, nutrient uptake by healthy tissue and nutrient uptake by tumor tissue as

$$\mathrm{P} = V_{\mathrm{p}}^{\mathrm{C}} \int_{\Omega} (p - p_{\mathrm{i}})\, \alpha\,(\sigma)\, c\mathcal{H}(c)\mathrm{d}\Omega, \tag{42}$$

$$\mathrm{U}^{\mathrm{H}} = V_{\mathrm{u}}^{\mathrm{H}} \int_{\Omega} \sigma\mathcal{H}(1-\phi)\mathrm{d}\Omega, \tag{43}$$

$$\mathrm{U}^{\mathrm{T}} = V_{\mathrm{u}}^{\mathrm{T}} \int_{\Omega} \sigma\phi\mathrm{d}\Omega, \tag{44}$$

respectively; refer to Eq. (7). The evolution of these three quantities over time for the two studied cases is shown in Fig. 5. At the very beginning, the nutrient is only released from the pre-existing vessel which carries blood due to the pressure difference between the inlet and the outlet (see Fig. 2a and Fig. 4a). Then, the nutrient production is approximately constant while the vasculature grows until the creation of the first loops ($t = 4.70\,\mathrm{d}$ in the first simulation and $t = 4.32\,\mathrm{d}$ in the second one), when it starts to grow. For every new loop, there is a jump in nutrient production followed by a rapid decrease, as α decreases in

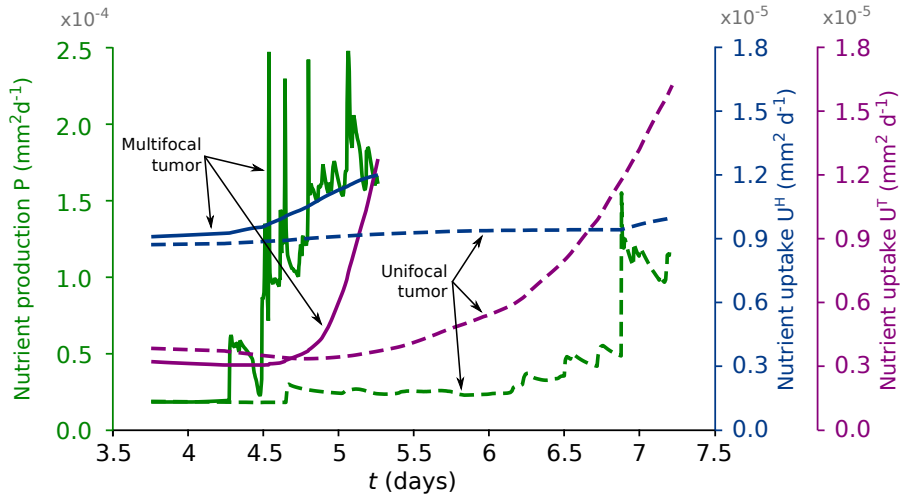

Figure 5. Nutrient production and nutrient uptake by the healthy and tumoral tissue in the unifocal and multifocal tumor simulations.

Eq. (42). In the simulation with one tumor, there are few and small jumps in nutrient production, except for one at $t = 6.91$ which represents the creation of the loop that encloses the tumor (Fig. 3c). Nutrient production in the simulation with the multifocal tumor is higher and more unsteady with four big jumps and several minor ones.

The initial amount of nutrient uptake by healthy tissue is larger than the uptake by the tumor tissue even if V_u^T is significantly larger than V_u^H. The reason for this is that the area occupied by healthy tissue is much larger than the tumor(s). We observe an increasing tendency in U^H over time, as uptake rates are directly proportional to the nutrient concentration which grows in healthy tissue for the time window of interest. This increase is more rapid in the simulation with the multifocal tumor due to the more connected vasculature. Also, the figure shows a kink in U^H at $t = 6.91$ d for the unifocal-tumor simulation due to the formation of a large loop in the vasculature that suddenly supplies nutrient to an ample region. We observe a similar but more pronounced tendency in U^T — almost constant nutrient uptake at the beginning, followed by a high increase after plenty of the released nutrient reaches the tumor interface. However, U^T experiences a faster increase due to much more functional loops when there are two tumors in the tissue.

4.3. Image-based simulation of vascular tumor growth and blood flow

We study tumor growth coupled with blood flow using realistic three-dimensional vasculature obtained from photoacoustic (PA) imaging [55]. Fig. 6a shows the vasculature and tumor cells at planes $x - y$ and $x - z$ from a PA image [55]. By selecting the most interesting region for simulation purposes (dashed-line rectangle) and setting a threshold to eliminate the background, we obtain the profile of the vessels and cancerous cells in three-dimensions from the grayscale image. In order to remove the noise in the obtained data, we filtered the image data by using a total-variation denoising algorithm and segmented it with a random walker. After that, we smoothed the image using a phase-field approach as described in Section 2.3. We finally placed an ellipsoidal microtumor at the center of the dashed circle. The result is shown in Fig. 6b. The aforementioned geometric configuration of the tumor and vasculature needs to be complemented with boundary conditions for the blood pressure. We classify the initial vessels into three trees marked in Fig. 6b with numbers I, II and III. The blood pressure through the vessel tree I takes value

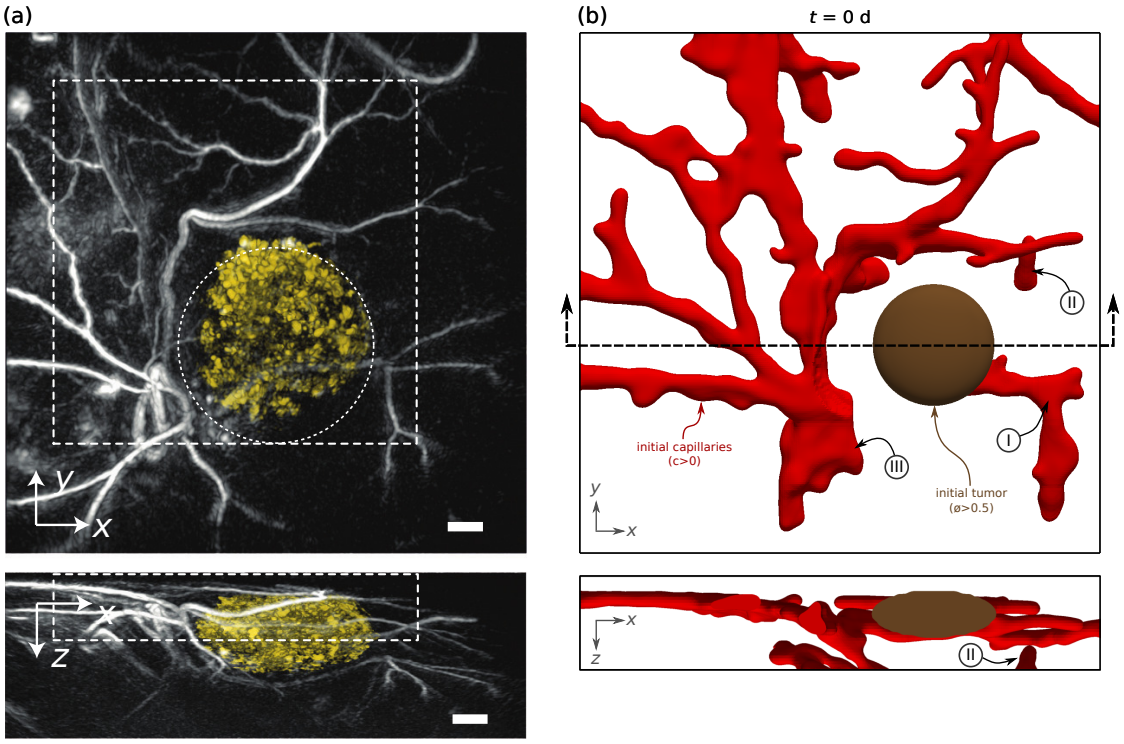

Figure 6. Initial conditions of the image-based simulation of vascular tumor growth and blood flow. (a) Photoacoustic images of the vasculature and the tumor taken from [55]. The white dashed circle around the tumor cells is 5.3 mm in diameter. The dashed white square highlights the region used in the simulation. Scale bar: 1mm. (b) Initial configuration for the simulation extracted using the algorithm described in Section 2.3. In order to adapt to the scale of our problem we reduce the computational domain to $650\,\mu\text{m} \times 650\,\mu\text{m} \times 117\,\mu\text{m}$. We use a computational mesh composed by $256 \times 256 \times 32$ C^1-quadratic elements. The initial capillary (red color) is formed by three disconnected vascular trees (labeled from I to III) that surround the tumor (brown color). The tumor is an ellipsoid with semi-axes $\{78, 78, 29.25\}\,\mu\text{m}$.

of $p = 1$ on the top face (in positive z direction). The pressures through tree III on the left, back and right faces, as well as that on the top face of tree II are fixed to be $p = 0$. We assume that the tumor is initially hypoxic.

We show in Fig. 7a-b the capillaries and tumor shape at $t = 0.72\,\text{d}$ and $t = 1.26\,\text{d}$, respectively. The cross sections at the bottom of both panels are taken through the initial tumor center. We also plot the pressure distribution on the surface of the vessels. Several capillaries are created from the three vessel trees at $t = 0.72\,\text{d}$. Similar to the two-dimensional case with one tumor, most TECs migrate towards the tumor center. And, although there are no anastomoses, two capillaries (from trees I and II) are close enough to produce flow due to their high pressure difference. Sufficient nutrient is released in this region to make tumor cells proliferative. The proliferation is more obvious in Fig. 7c-d where we plot the tumor and the proliferative and hypoxic regions for the same time steps (note that the tumor is upside-down for the sake of visibility). From both figures, we observe that cancerous cells proliferate along negative y and positive z directions. At $t = 1.26\,\text{d}$, we find functional blood vessel loops that connect trees I and II. These connections boost the growth of the tumor. Indeed, as shown in Fig. 7e, the tumor volume follows an initially decreasing tendency followed by a rapid increase: First, at $t = 0\,\text{d}$, all tumor cells are hypoxic and

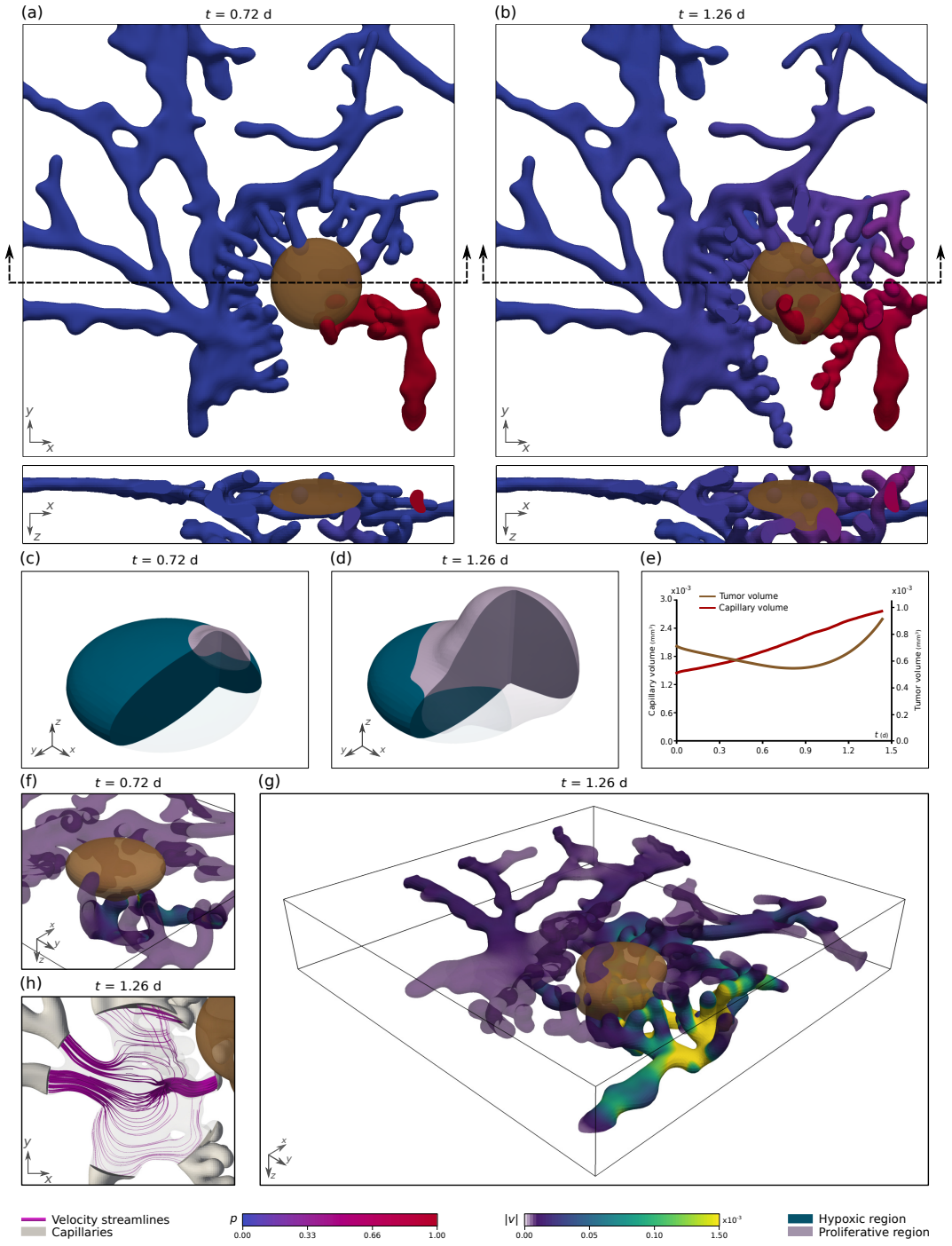

Figure 7. Image-based simulation of vascular tumor growth and blood flow. (a)–(b) Top view and cross section of the computational domain showing the pressure distribution at the capillary wall at $t = 0.72$ d and $t = 1.26$ d. (c)–(d) Three-dimensional view of the tumor at $t = 0.72$ d and $t = 1.26$ d highlighting the proliferative and hypoxic regions. A section of the tumor has been removed to visualize its interior. Note that due to the high amount of nutrient there is no necrotic region. (e) Plot of the capillary and tumor volume over time. (f)–(g) Blood velocity at the capillaries at $t = 0.72$ d and $t = 1.26$ d. The highest velocities are located in the connection of vascular trees I and II. (h) Velocity streamlines at $t = 1.26$ d inside the capillaries (gray color) in the proximity of the tumor. The radii of the streamlines are proportional to the velocity magnitude.

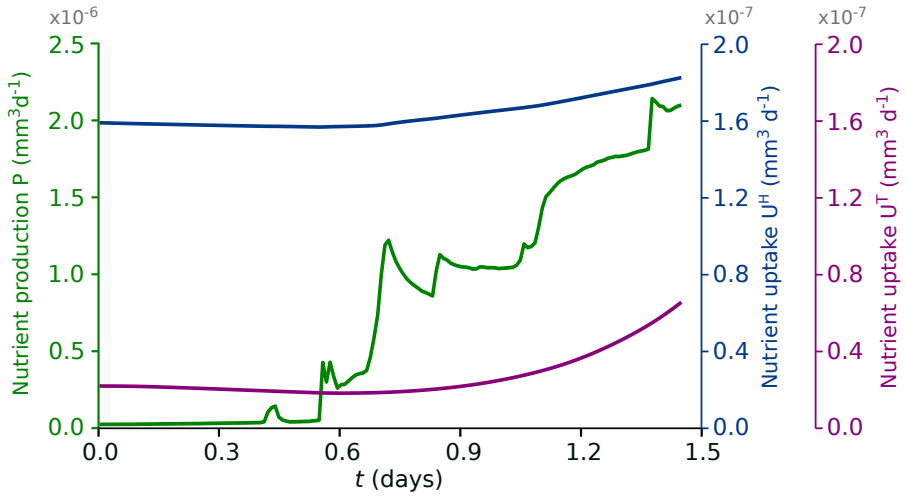

Figure 8. Nutrient production and nutrient uptake by the healthy and tumoral tissue in the image-based three-dimensional simulation.

consume nutrient at a high rate. Thus, the tumor undergoes a slight shrinkage due to low nutrient level. Then, by $t = 0.72$ d, although proliferative cancerous cells start to invade the adjacent tissue, the growth is only local and the total tumor volume still decreases. At $t = 0.84$ d, the provided nutrient is sufficient to make tumor growth dominant. Thereafter, the tumor continues its growth at faster speeds. Note that the capillary volume increases during the entire simulation as shown in Fig. 7e. This is because angiogenesis is activated at a very early stage, approximately around $t = 0.1$ d.

In Figs. 7f and 7g we plot the velocity magnitude on the surface of capillaries at $t = 0.72$ d and $t = 1.26$ d, respectively. Note that for visualization purposes we have added a transparent gradient to the velocity distribution color scale, so that the poorly perfused capillaries are semi-transparent. Fig. 7f shows a zoomed region of the tissue near the tumor where we can observe capillaries with low blood velocities (the only ones in the domain at this time step). This flow is responsible for the local growth seen in Fig. 7c. In the second figure, the vascular network is better connected and the blood is flowing rapidly through many capillaries. We show in Fig. 7h streamlines of the velocity field that start inside the capillary on the middle right of the figure, go through a wide vessel structure and bifurcate to other capillaries. The radius of the streamlines varies with the velocity. The image shows how blood slows down in regions with higher diameter, like the wide vessel structure at the center of the figure, and increases in thinner capillaries, as in the left and right capillaries of the figure. Finally, analyzing the nutrient production and uptake using Eqs. (42) to (44) (see Fig. 8) we observe a pattern similar to that of the two-dimensional examples: the production peaks and decreases whenever a new loop appears and the overall production has an increasing tendency. We can see from the curve that the first loop is formed around $t = 0.42$ d which connects vascular trees I and II.

5. Conclusion

We have presented a computational framework for the dynamics of vascular tumor growth coupled with a simplified model of 3D blood flow on a time-evolving capillary network. The proposed method

avoids the mesh-generation bottleneck of 3D blood flow computations and can be integrated with imaging data, opening new possibilities to study the tumor microenvironment.

The model successfully reproduced the heterogeneity and unsteadiness of blood flow in the tumor microenvironment. Our simulations indicate that the changing nature of blood flow is highly controlled by newly created anastomoses that drastically alter the flow dynamics, and create new irrigated areas in the tissue. The severity of the changes depends on the pressure difference between the connecting capillaries. Our computations suggest an scenario in which tumor growth depends on a delicate balance between different microenvironmental conditions. For example, the model predicted that two nearby tumors were able to cooperate and grow faster than a unifocal tumor of the same size. The 3D simulation that we presented shows how our model can be seamlessly integrated with *in vivo* imaging data to study angiogenesis and tumor growth. The use of images at different time points may permit to estimate the model parameters with *in vivo* information, opening the possibility of truly predictive simulations.

6. Acknowledgments

This work was supported by the European Research Council through the FP7 Ideas Starting Grant program (Contract # 307201). This support is gratefully acknowledged. Jiangping Xu also thanks the starting grant supported by Jiangsu University (Grant # 4111110015).

Appendix A. Parameters

We summarize in Table A.1 the dimensionless values of the parameters used in the model. The physical values of the parameters may be obtained using the length scale $L_s = 1.25\,\mu m$ and time scale $T_s = 1562.5\,s$. Most of them were obtained from either *in vivo* or *in vitro* observations or were previously used in mathematical models; otherwise we give a justification for the selected parameter values.

The diffusion coefficient of TAF is set to $D_f = 1 \times 10^{-9}\,cm^2\,s^{-1}$ following [40, 56, 57]. The mobility of the phase-field that defines the location of capillaries (M_c) and the proliferation rate of endothelial cells (B_p) set the time scale of the dynamics of capillaries, which is slower than the dynamics of TAF. We set the ratio D_f/M_c, so that $M_c = 1.002 \times 10^{-11}\,cm^2\,s^{-1}$ and $B_p = 1.401$ following [43]. In addition, the tumor angiogenic factor threshold for highest proliferation is defined following the parametric study in [57]. As capillaries develop faster than tumors we set the ratio between the mobility of the phase-field of the tumor and the capillaries to $M_\phi/M_c = 0.3$. The diffusion, production and uptake rates of the nutrient have been set following [19]. We tested several sets of these parameters and compared the resulting tumor dynamics with experimental time scales observed in the avascular stages. In addition, there is experimental evidence that shows that $V_u^T >> V_u^H$ [58]. The radius of an endothelial cell R is set to $5\,\mu m$, which is within the range of measured values [59]. The length scale λ_c is proportional to the capillary wall. We set its value to $1.25\,\mu m$ so that the wall thickness is of the order of $1\,\mu m$ [60]. The length scale λ_ϕ controls to the interface width of the tumors. In the model, we consider solid, highly packaged tumors composed by non-invasive cells that cannot migrate away of the solid mass. The thickness of the tumor interface should be less than the radius of a cell, so we set $\lambda_\phi = 2\sqrt{2}$ which is approximately half of R. For the three-dimensional computations, R has been increased within the physiological range for computational reasons (and consequently λ_c and λ_ϕ).

The uptake rate of TAF by capillaries has been set following [43] to $B_u = D_f/R^2$, so that the TAF penetration into a capillary is limited to the radius of a cell R. We have set the tumor angiogenic factor condition for TEC activation f_{act} and the natural decay rate δ so that hypoxic cells located farther than $200\,\mu m$ away from a capillary can activate TECs, which is within the physiological range the nutrient

Table A.1. *In silico* values of the parameters used in the proposed model. The physical values of the parameters may be obtained using the length scale $L_s = 1.25\,\mu$m and time scale $T_s = 1562.5$ s. In three-dimensional example, we take the values $R = 8$, $\lambda_c = \sqrt{2}$ and $\lambda_\phi = 2$ to be able to use a coarser mesh.

Parameter	Description	Unit	*In silico* value
M_c	Mobility of endothelial cells	$[L^2T^{-1}]$	1
λ_c	Interface width of capillaries	[L]	1
B_p	Proliferation rate of endothelial cells	$[T^{-1}]$	1.401
f_p	TAF threshold for highest proliferation	[-]	0.3
R	TEC radius	[L]	4
c_{act}	Condition 1 for TEC (de)activation	[-]	0.9
f_{act}	Condition 2 for TEC (de)activation	[-]	0.001
χ	Chemotactic constant	$[LT^{-1}]$	7.28
δ_4	Dll4 effective distance	[L]	80
D_σ	Diffusion coefficient of the nutrient	$[L^2T^{-1}]$	30
V_p^C	Permeability of the capillaries	$[TLM^{-1}]$	1
V_u^T	Uptake rate of nutrient by tumor	$[T^{-1}]$	0.006
V_u^H	Uptake rate of nutrient by host tissue	$[T^{-1}]$	0.0006
v_p	Threshold for describing blood flow	[-]	0.000002
M_ϕ	Reference mobility of the tumor	$[T^{-1}]$	0.3
λ_ϕ	Interface width of tumor	[L]	$\sqrt{8}$
ϵ_m	Parameter of the tilting function	[-]	0.01
σ^*	Breaking point of the tilting function	[-]	0.48
σ^s	Related with the width of the tilting function	[-]	0.05
$\sigma^{n\text{-}h}$	Necrotic/hypoxic nutrient threshold	[-]	0.2
$\sigma^{h\text{-}v}$	Hypoxic/viable nutrient threshold	[-]	0.4
$\sigma_{ref}^{\mathcal{G}}$	Reference nutrient concentration for the TAF production function	[-]	$1/\sqrt{125}$
$\mathcal{G}_{ref}$	Reference value for TAF production rate	$[T^{-1}]$	0.008
D_f	Diffusion coefficient of TAF	$[L^2T^{-1}]$	100
B_u	Uptake rate of TAF by capillaries	$[T^{-1}]$	6.25
δ	Natural decay rate of TAF	$[T^{-1}]$	0.0005

diffusion length. The numerical parameters ϵ_m, σ^* and σ^s are set to verify the condition $|m(\sigma)| < 1/3$; see [46]. $\sigma_{ref}^{\mathcal{G}}$ and $\mathcal{G}_{ref}$ are also numerical parameters whose values are set so that the TAF production rate peaks at the hypoxic region and decays exponentially to zero at the necrotic and proliferative areas of the tumor [19]. The parameters $\sigma^{n\text{-}h} = 0.2$ and $\sigma^{h\text{-}v} = 0.4$ delimit these regions, so that when the nutrient is between 20% and 40% of the maximum amount of nutrient, cells are hypoxic and their production rate is above 30% of the maximum [19]. Furthermore, we have set δ_4 to $20R$, so that TECs impede the activation of other TECs in their neighborhood. This value guarantees that the density of capillaries is similar to that observed in experiments as shown in previous works; this was also tested through numerical simulations. By setting the chemotactic speed χ to $0.503\,\mathrm{mm\,d^{-1}}$, we obtain TEC velocity values within the range observed in [61, 62].

References

[1] D. Hanahan, R. A. Weinberg, Hallmarks of cancer: The next generation, Cell 144 (2011) 646–674.

[2] J. Folkman, Tumor angiogenesis: therapeutic implications, N. Engl. J. Med. (1971) 1182–6.
[3] W. D. Figg, J. Folkman, Angiogenesis: An integrative approach from science to medicine, Springer, 2011.
[4] S. Goel, D. G. Duda, L. Xu, L. L. Munn, Y. Boucher, D. Fukumura, R. K. Jain, Normalization of the vasculature for treatment of cancer and other diseases., Physiol. Rev. 91 (2011) 1071–1121.
[5] J. M. Rutkowski, M. A. Swartz, A driving force for change: interstitial flow as a morphoregulator, Trends Cell Biol. 17 (2007) 44 – 50.
[6] J. D. Martin, D. Fukumura, D. G. Duda, Y. Boucher, R. K. Jain, Reengineering the tumor microenvironment to alleviate hypoxia and overcome cancer heterogeneity, Cold Spring Harbor Perspec. Med. (2016).
[7] S. Sanga, H. B. Frieboes, X. Zheng, R. Gatenby, E. L. Bearer, V. Cristini, Predictive oncology: A review of multidisciplinary, multiscale *in silico* modeling linking phenotype, morphology and growth, NeuroImage 37 (2007) S120 – S134.
[8] T. E. Yankeelov, G. An, O. Saut, E. G. Luebeck, A. S. Popel, B. Ribba, P. Vicini, X. Zhou, J. A. Weis, K. Ye, G. M. Genin, Multi-scale modeling in clinical oncology: Opportunities and barriers to success, Ann. Biomed. Eng. 44 (2016) 2626–2641.
[9] G. Lorenzo, M. A. Scott, K. Tew, T. J. R. Hughes, Y. J. Zhang, L. Liu, G. Vilanova, H. Gomez, Tissue-scale, personalized modeling and simulation of prostate cancer growth, Proc. Natl. Acad. Sci. (2016) 201615791.
[10] J. Wu, Q. Long, S. Xu, A. R. Padhani, Y. Jiang, Simulation of 3D solid tumor angiogenesis including arteriole, capillary, and venule, Mol. Cell. Biomech. 5 (2008) 1–23.
[11] H. B. Frieboes, F. Jin, Y.-L. Chuang, S. M. Wise, J. S. Lowengrub, V. Cristini, Three-dimensional multispecies nonlinear tumor growth - II: tumor invasion and angiogenesis, J. Theor. Biol. 264 (2010) 1254–1278.
[12] A. R. Pries, T. W. Secomb, P. Gaehtgens, J. F. Gross, Blood flow in microvascular networks: experiments and simulation, Circ.Res. 67 (1990) 826–834.
[13] A. R. Pries, T. W. Secomb, T. Geβner, M. B. Sperandio, J. F. Gross, P. Gaehtgens, Resistance to blood and flow in microvessels and *in vivo*, Circ.Res. 75 (1994) 904–915.
[14] A. R. Pries, T. W. Secomb, P. Gaehtgens, Structural adaptation and stability of microvascular networks: theory and simulations, Am. J. Physiol.-Heart Circul. Physiol. 275 (1998) H349–H360.
[15] A. R. Pries, B. Reglin, T. W. Secomb, Structural adaptation of microvascular networks: functional roles of adaptive responses, Am. J. Physiol.-Heart Circul. Physiol. 281 (2001) H1015–H1025.
[16] F. Cassot, F. Lauwers, C. Fouard, S. Prohaska, V. Lauwers-Cances, A novel three-dimensional computer-assisted method for a quantitative study of microvascular networks of the human cerebral cortex, Microcirculation 13 (2006) 1–18.
[17] J. Reichold, M. Stampanoni, A. L. Keller, A. Buck, P. Jenny, B. Weber, Vascular graph model to simulate the cerebral blood flow in realistic vascular networks, J. Cereb. Blood Flow Metab. 29 (2009) 1429–1443.
[18] S. Lorthois, F. Cassot, F. Lauwers, Simulation study of brain blood flow regulation by intra-cortical arterioles in an anatomically accurate large human vascular network. Part II: flow variations induced by global or localized modifications of arteriolar diameters, Neuroimage 54 (2011) 2840–2853.
[19] J. Xu, G. Vilanova, H. Gomez, Full-scale, three-dimensional simulation of early-stage tumor growth: The onset of malignancy, Comput. Meth. Appl. Mech. Eng. (2016).
[20] E. A. B. F. Lima, J. T. Oden, R. C. Almeida, A hybrid ten-species phase-field model of tumor growth, Math. Models Methods Appl. Sci. 24 (2014) 2569–2599.
[21] T. Panitanarak, S. M. Shontz, A parallel log barrier-based mesh warping algorithm for distributed memory machines, Engineering with Computers 34 (2018) 59–76.
[22] S. K. Stoter, P. Müller, L. Cicalese, M. Tuveri, D. Schillinger, T. J. R. Hughes, A diffuse interface method for the Navier–Stokes/Darcy equations: Perfusion profile for a patient-specific human liver based on MRI scans, Comput. Meth. Appl. Mech. Eng. 321 (2017) 70–102.
[23] H. Gomez, M. Bures, A. Moure, A review on computational modelling of phase-transition problems, Philos. T. R. Soc. A 377 (2019) 20180203.
[24] L.-Q. Chen, Phase-field models for microstructure evolution, Annu. Rev. Mater. Sci. 32 (2002) 113–140.
[25] A. J. Bray, Theory of phase-ordering kinetics, Adv. Phys. 51 (2002) 481–587.
[26] W. J. Boettinger, J. A. Warren, C. Beckermann, A. Karma, Phase-field simulation of solidification, Ann. Rev. Mater. Res. 32 (2002) 163–194.
[27] I. Steinbach, Phase-field models in materials science, Model. Simul. Mater. Sci. Eng. 17 (2009) 073001.
[28] H. M. Byrne, L. Preziosi, Modelling solid tumour growth using the theory of mixtures, Math. Med. Biol. 20 (2003) 341–366.
[29] J.-F. Lu, Y.-P. Tan, J.-H. Wang, A phase field model for the freezing saturated porous medium, Int. J. Eng. Sci. 49 (2011) 768 – 780.
[30] D. Mokbel, H. Abels, S. Aland, A phase-field model for fluid-structure interaction, J. Comput. Phys. 372 (2018) 823 – 840.
[31] J. Bueno, H. Casquero, Y. Bazilevs, H. Gomez, Three-dimensional dynamic simulation of elastocapillarity, Meccanica 53 (2018) 1221–1237.
[32] X. Li, J. S. Lowengrub, A. Rätz, A. Voigt, Solving pdes in complex geometries: A diffuse domain approach, Commun. Math. Sci. 7 (2009) 81.
[33] J. Parvizian, A. Düster, E. Rank, Finite cell method, Comput. Mech. 41 (2007) 121–133.
[34] K. Tsuboi, Incompressible flow simulation of complicated boundary problems with rectangular grid system, Theo. Appl.

Mech. 40 (1991) 297–309.
[35] S. Osher, R. Fedkiw, Level set methods and dynamic implicit surfaces, volume 153, Springer Science & Business Media, 2006.
[36] B. D. Coleman, W. Noll, The thermodynamics of elastic materials with heat conduction and viscosity, Arch. Ration. Mech. Anal. 13 (1963) 167–178.
[37] M. Potente, H. Gerhardt, P. Carmeliet, Basic and therapeutic aspects of angiogenesis, Cell 146 (2011) 873–887.
[38] M. Knowles, P. Selby, Introduction to the cellular and molecular biology of cancer, Oxford University Press Inc., 2005.
[39] J. Xu, G. Vilanova, H. Gomez, A mathematical model coupling tumor growth and angiogenesis, PLoS One 53 (2016) 449–464.
[40] G. Vilanova, I. Colominas, H. Gomez, Capillary networks in tumor angiogenesis: From discrete endothelial cells to phase-field averaged descriptions via isogeometric analysis, Int. J. Numer. Meth. Biomed. 29 (2013) 1015–1037.
[41] M. Hellström, L.-K. Phng, J. J. Hofmann, E. Wallgard, L. Coultas, P. Lindblom, J. Alva, A.-K. Nilsson, L. Karlsson, N. Gaiano, et al., Dll4 signalling through notch1 regulates formation of tip cells during angiogenesis, Nature 445 (2007) 776–780.
[42] H. Gerhardt, M. Golding, M. Fruttiger, C. Ruhrberg, A. Lundkvist, A. Abramsson, M. Jeltsch, C. Mitchell, K. Alitalo, D. Shima, C. Betsholtz, VEGF guides angiogenic sprouting utilizing endothelial tip cell filopodia, J. Cell Biol. 161 (2003) 1163–1177.
[43] G. Vilanova, I. Colominas, H. Gomez, A mathematical model of tumour angiogenesis: growth, regression and regrowth, J. R. Soc. Interface 14 (2017) 20160918.
[44] J. W. Baish, P. A. Netti, R. K. Jain, Transmural coupling of fluid flow in microcirculatory network and interstitium in tumors, Microvasc. Res. 53 (1997) 128–141.
[45] L. T. Baxter, R. K. Jain, Transport of fluid and macromolecules in tumors I. Role of interstitial pressure and convection, Microvasc. Res. 37 (1989) 77–104.
[46] R. Kobayashi, A brief introduction to phase field method, volume 1270, Dalian, pp. 282–291. Conference of 14th International Summer School on Crystal Growth, ISSCG14.
[47] P. Carmeliet, R. K. Jain, Molecular mechanisms and clinical applications of angiogenesis, Nature 473 (2011) 298–307.
[48] D. J. Hicklin, L. M. Ellis, Role of the vascular endothelial growth factor pathway in tumor growth and angiogenesis, J. Clin. Oncol. 23 (2005) 1011–1027.
[49] A. Beenken, M. Mohammadi, The FGF family: biology, pathophysiology and therapy, Nat. Rev. Drug. Discov. 8 (2009) 235–253.
[50] M. O. Bernabeu, M. L. Jones, J. H. Nielsen, T. Krüger, R. W. Nash, D. Groen, S. Schmieschek, J. Hetherington, H. Gerhardt, C. A. Franco, P. V. Coveney, Computer simulations reveal complex distribution of haemodynamic forces in a mouse retina model of angiogenesis, J. R. Soc. Interface 11 (2014) 20140543.
[51] K. Saeed, M. Tabedzki, M. Rybnik, M. Adamski, K3M: A universal algorithm for image skeletonization and a review of thinning techniques, Int. J. Appl. Math. Comput. Sci. 20 (2010) 317–355.
[52] H. Gomez, V. M. Calo, Y. Bazilevs, T. J. R. Hughes, Isogeometric analysis of the Cahn–Hilliard phase-field model, Comput. Meth. Appl. Mech. Eng. 197 (2008) 4333–4352.
[53] H. Gomez, T. J. R. Hughes, X. Nogueira, V. M. Calo, Isogeometric analysis of the isothermal Navier-Stokes-Korteweg equations, Comput. Meth. Appl. Mech. Eng. 199 (2010) 1828–1840.
[54] K. E. Jansen, C. H. Whiting, G. M. Hulbert, A generalized-α method for integrating the filtered Navier-Stokes equations with a stabilized finite element method, Comput. Meth. Appl. Mech. Eng. 190 (2000) 305 – 319.
[55] A. P. Jathoul, J. Laufer, O. Ogunlade, B. Treeby, B. Cox, E. Zhang, P. Johnson, A. R. Pizzey, B. Philip, T. Marafioti, et al., Deep *in vivo* photoacoustic imaging of mammalian tissues using a tyrosinase-based genetic reporter, Nat. Photonics 9 (2015) 239–246.
[56] R. C. Schugart, A. Friedman, R. Zhao, C. K. Sen, Wound angiogenesis as a function of tissue oxygen tension: A mathematical model, Proc. Natl. Acad. Sci. 105 (2008) 2628–2633.
[57] R. D. M. Travasso, E. C. Poiré, M. Castro, J. C. Rodríguez-Manzaneque, A. Hernández-Machado, Tumor angiogenesis and vascular patterning: A mathematical model, PLoS One 6 (2011) e19989.
[58] A. Ramanathan, C. Wang, S. L. Schreiber, Perturbational profiling of a cell-line model of tumorigenesis by using metabolic measurements, Proc. Natl. Acad. Sci. 102 (2005) 5992–5997.
[59] S. Gebb, T. Stevens, On lung endothelial cell heterogeneity, Microvasc. Res. 68 (2004) 1 – 12.
[60] Y.-T. Shiu, J. A. Weiss, J. B. Hoying, M. N. Iwamoto, I. S. Joung, C. T. Quam, The role of mechanical stresses in angiogenesis, Crit. Rev. Biomed. Eng. 33 (2005) 431–510.
[61] H. Brem, J. Folkman, Inhibition of tumor angiogenesis mediated by cartilage, J. Exp. Med. 141 (1975) 427–439.
[62] L. Jakobsson, C. A. Franco, K. Bentley, R. T. Collins, B. Ponsioen, I. M. Aspalter, I. Rosewell, M. Busse, G. Thurston, A. Medvinsky, S. Schulte-Merker, H. Gerhardt, Endothelial cells dynamically compete for the tip cell position during angiogenic sprouting, Nat. Cell Biol. 12 (2010) 943–953.